

A Survey for Cool White Dwarfs and the age of the Galactic Disc

R.A. Knox¹, M.R.S. Hawkins^{1,2}, N.C. Hambly^{1,2}

¹*Institute for Astronomy, University of Edinburgh, Blackford Hill, Edinburgh, EH9 3HJ*

²*Royal Observatory, Blackford Hill, Edinburgh, EH9 3HJ*

Accepted —. Received —; in original form —

ABSTRACT

We describe a new multi-colour proper motion survey for cool white dwarfs (CWDs). The observational database consists of ~ 300 digitally scanned Schmidt plates in ESO/SERC field 287. The entire survey procedure, from the raw Schmidt plate data to final white dwarf luminosity function (WDLF) is described, with special emphasis on completeness concerns.

We obtain a sample of 58 WDs, for which we have follow up CCD photometry and spectroscopy of a representative sub-sample. Effective temperatures and luminosities of our sample objects are determined by comparing photometry with the model atmosphere predictions of Bergeron, Saumon and Wesemael. Space densities are calculated using an adaptation of Schmidts ($1/V_{max}$) method, from which a WDLF is constructed. Comparison of our observational LF with the models of both Wood and García-Berro et al. indicate an age for the local Galactic Disc of 10_{-1}^{+3} Gyr. Importantly, we find no evidence of incompleteness in our survey sample. Proper motion number counts imply the survey is complete, and the WD sample passes the (V/V_{max}) completeness test.

Key words: surveys – stars: luminosity function – white dwarfs

1 INTRODUCTION

A reliable age for the local Galactic Disc places a valuable constraint on both globular cluster ages and cosmological models. A number of independent methods of investigating this problem have been employed in the past (eg. Jimenez 1998 and references therein), resulting in a broad consensus that the lower limit for the Disc age lies between 8 and 12 Gyr. Potentially one of the most reliable means of estimating the Disc age is via cool white dwarf (CWD) stars. These estimates use the idea, first proposed by Schmidt (1959), that in a galaxy of finite age there will be a temperature beyond which the oldest, coolest white dwarfs (WDs) have not had time to cool. This predicted cut-off in the luminosity function (LF) of WDs, if satisfactorily observed, can then be used in conjunction with WD cooling models to derive the Disc age.

CWDs are difficult to find, being both extremely faint and of similar colour to the numerous K and M-type dwarfs; and are almost exclusively discovered by means of their proper motion. The cut-off in the WDLF was observed (Liebert, Dahn & Monet 1988, hereafter LDM) after thorough follow up observations of CWD candidates drawn from the Luyten Half Second (LHS) Catalogue (Luyten 1979). Although at that time a Disc age of 9.3 ± 2 Gyr was de-

rived from this sample (Winget et al. 1987), further observations and improvements in model atmospheres (Bergeron, Ruiz & Leggett 1997, hereafter BRL) and theoretical LFs (Wood 1992, 1995) has prompted a recent re-determination of the Disc age for the same sample (Leggett, Ruiz & Bergeron 1998, hereafter LRB), yielding a value of 8 ± 1.5 Gyr. While the existence of the cut-off in the LDM WDLF has not been challenged by subsequent observational work, the details of its precise position and shape have. A sample of CWDs found using common proper motion binaries (CPMBs), again culled from the Luyten surveys, suggest that there are ~ 5 times more very faint CWDs than found by LDM (Oswalt et al. 1996, hereafter OSWH). A Disc age of 9.5 ± 1 Gyr was found using this sample, and the factor of ~ 5 increase in the faintest WDs has been confirmed by an independent search for CWDs in the south (Ruiz and Takamiya 1995).

Until now, the proper motion catalogues used to extract samples of CWDs have been produced by ‘blink’ comparison. While these surveys have clearly been successful in picking up individual stars of low luminosity and high proper motion, the use of such a subjective survey technique raises worries concerning completeness. The advent of high precision micro-densitometers such as SuperCOSMOS (Hambly 1998 and references therein) allow proper motions

arXiv:astro-ph/9903345v1 23 Mar 1999

and magnitudes to be calculated objectively using a series of plates in the same field. Hambly et al. (1997) have recently discovered in Taurus perhaps the coolest known WD using just such a procedure. This object, WD 0346+246, should certainly appear in the LHS Catalogue, and would then presumably have been included in the LDM sample since it fulfills the given criteria. This object was discovered serendipitously from work in a particular $6 \times 6^\circ$ Schmidt field, and therefore casts further doubt on the completeness of the Luyten catalogue.

In this work we exploit both the extensive collection of over 300 plates in ESO/SERC field 287 and the power of the SuperCOSMOS measuring machine to produce a deep, complete multi-colour proper motion survey from which a sample of CWDs has been extracted. Much attention was given to the critical question of completeness, with specific reference to the choice of survey limits and the sources of potential contaminants. The paper is organised as follows: the plate database and reduction of the digitally scanned data is described in Section 2; the choice of survey limits to combat sample contamination and the method of WD sample selection are discussed in Section 3; in Section 4 the important question of the high proper motion limit is addressed by independent tests; some follow up observations of our WD candidates are presented in Section 5; stellar parameters are calculated for our sample in Section 6, which also includes a discussion of potential contaminant populations; the WDLF from our sample is presented in Section 7, and the derived Disc ages discussed in Section 8.

2 SCHMIDT PLATE DATA REDUCTION

In the course of a long term quasar variability study (eg. Véron & Hawkins 1995) over 300 Schmidt plates have been taken in ESO/SERC field 287. Figure 1 shows the distribution over time of the plate collection in this field in the two principal passbands available, B_J and R_F . Additional plate material exists in the U (19 plates), V (11 plates) and I (40 plates) passbands. All these plates have been digitally scanned by either the SuperCOSMOS plate measuring machine or its predecessor COSMOS (MacGillivray and Stobie, 1984). As described in Appendix A, a CWD survey utilising the reduced proper motion (RPM) population discrimination technique requires photometry in at least two passbands and proper motion data. Although for most stellar types a survey of this sort will be proper motion limited, for extremely intrinsically faint objects such as cool degenerates the photometric survey limits also become important. A principal concern in this work is therefore to maximise the survey depth.

The technique of stacking digitised Schmidt plates has been in existence for some time (eg. Hawkins 1991; Kemp & Meaburn 1993; Schwartzberg et al. 1996), and has recently been thoroughly investigated with SuperCOSMOS (Knox et al. 1998). The database presented in Figure 1 is an obvious candidate for stacking in a proper motion survey, since at least 4 plates are available in most years and the use of 4 plate stacks rather than single plate data will yield deeper photometric survey limits with no reduction in the proper motion time baseline. The data has therefore been grouped into 4 plate stacks according to Table 1.

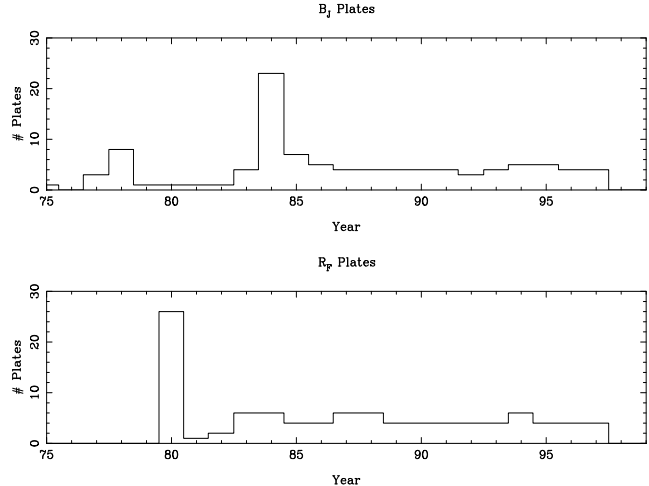


Figure 1. Number of plates per year in ESO/SERC Field 287 in the B_J (top) and R_F (bottom) passbands

Year	B_J	R	Year	B_J	R	Year	B_J	R
1977	1		1984	4	2	1991	1	1
1978	1		1985	2	1	1992	1	1
1979			1986	1	1	1993	1	1
1980		5	1987	1	1	1994	1	1
1981			1988	1	1	1995	1	1
1982			1989	1	1	1996	1	1
1983	1	1	1990	1	1			

Table 1. The number of B_J and R 4 plate stacks per annual epoch.

In order to track objects through epochs and calculate relative proper motions, all the stacks have been shifted to a common co-ordinate system corresponding to a measure of the high quality B_J plate J3376. This is achieved by a global transformation followed by local transformations (translation, rotation and scale), performed by splitting the stack area into a grid of 16×16 small areas (Hawkins 1986). Every object in each area is used to define the local transformation (since fainter objects are more numerous, they essentially define the astrometric coordinate system). Objects are then paired up between epochs. The software used in this work operates using a fixed ‘box size’ (13arcsecs) in which it looks for a pair, thus in the first instance a high proper motion limit is imposed on the survey – this issue will be addressed in detail later. The pairing procedure yields a list of x and y coordinates for each object, one set for each stack the object is found on. Calculating proper motions is then simply a matter of performing a linear regression fit to each object’s x and y coordinates as a function of time. However, erroneous pairing inevitably occurs between stacks, and we therefore wish to perform some form of bad point rejection to reduce contamination by spurious proper motions. In order to reject deviant points (and calculate parameters such as σ_μ and χ^2) an estimate of the error associated with each measure of position is required. We assume this error is simply a function of magnitude and that it will vary from stack to stack, but not across the survey area. This error is calculated using the

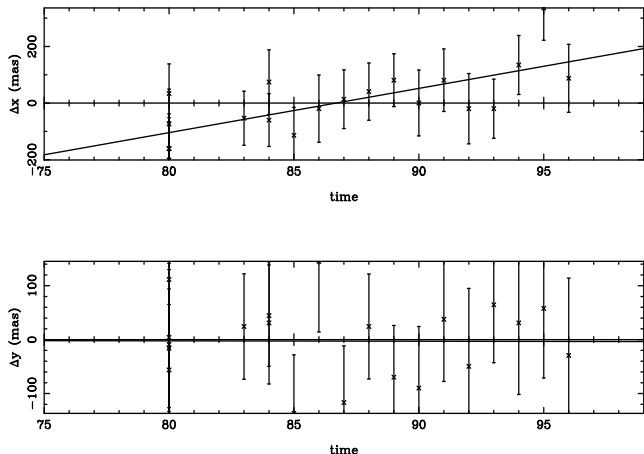


Figure 2. An example of a linear regression fit to a set of object positions. The vertical axis is deviation of measured position on a given stack from the mean object position, with year this century on the horizontal axis

deviation of an object’s position on a particular stack from the mean position over the 20 stacks used, and is determined over 10 magnitude bins. A 3σ iterative rejection procedure is implemented to reject spurious pairings or high proper motion objects which are not reflecting the true positional errors sought. The calculated errors are much as one might expect: decreasing for brighter objects until factors such as saturation and blended images makes positional measures more uncertain.

A straight line fit can now be applied to the x and y data for each object, the gradient of which is taken to be the measured proper motion, μ_x and μ_y respectively. An example is shown in Figure 2, the points showing the deviation at each epoch from the average object position with error bars calculated as above. Deviant points arising from spurious pairings often lie far from the other data and will give rise to spurious high proper motion detections if not removed. We therefore iteratively remove points lying 3σ from the fitted line. This can occasionally lead to further problems if there are several bad points associated with the object, and the result of several iterations can be a larger spurious motion detection. This source of contamination is generally eliminated by insisting sample objects are detected on virtually every stack. The validity of the positional error estimation scheme described above has been verified by confirming that scatter plots of log reduced χ^2 as a function of magnitude cluster around zero for all magnitudes in all regions of the survey area.

Instrumental magnitudes are calculated for every object detected on each stack in the standard COSMOS/SuperCOSMOS fashion (Beard et al. 1990 and references therein). Briefly, an object detection is defined by a given number of interconnected pixels with intensity above a given threshold (eg. 8 interconnected pixels with intensity above a 2.5σ sky noise threshold for SuperCOSMOS data). An object’s instrumental magnitude is then calculated as the log of the sum of the intensity above background across the object area. This quantity varies monotonically with true magnitude, and is therefore suitable for use in construct-

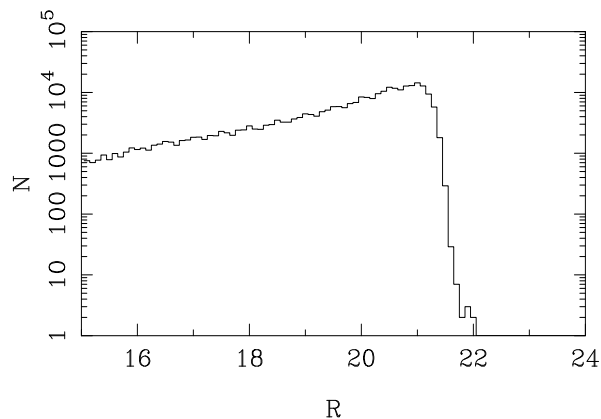


Figure 3. Number counts as a function of apparent R magnitude

ing calibration curves using a CCD sequence. A sequence of ~ 200 stars with CCD magnitudes measured in a variety of passbands exists in field 287 (Hawkins et al. 1998), yielding U, B, V, R and I photometry to a typical accuracy of 0.15 magnitudes (see Section 5.2). Significantly smaller errors are theoretically obtainable from photographic material, and the larger uncertainties we find appear to be caused by systematic deviations of sequence objects from the calibration curve. This is not a colour or field effect, and is probably caused by differences in detection media.

3 SURVEY LIMITS AND SAMPLE SELECTION

The ‘catalogue’ resulting from the implementation of the procedure described in the previous section consists of astrometric and photometric measures for over 200,000 objects. Criteria for inclusion in this preliminary sample is merely detection in both B_J and R passbands (since these are required for construction of the reduced proper motion diagram (RPMD)) and a measure of proper motion in both these passbands. It is from these objects that an uncontaminated proper motion sample is to be drawn; and we require well defined universal survey limits so that space densities can be calculated from the final survey sample.

Number count plots from this survey data increase linearly with increasing magnitude, as shown for the R data in Figure 3, before dropping precipitously. This cut-off is attributed to the survey detection limit, and the position of the turnover is used to determine photometric survey limits. The limits used are 21.2 in R and 22.5 in B.

The proper motion distribution for all objects in our survey area detected on at least 15 stacks in both B and R is shown in Figure 4. Low proper motions are generally an artifact of measuring machine error, thus the distribution indicates a typical error in measured proper motions of $\sim 10\text{mas/yr}$. Our criteria for choosing a survey proper motion limit are elimination of contaminant spurious proper motions from the sample and, with this in mind, maximising the size of the final proper motion sample extracted. The deterioration of positional accuracy with magnitude means

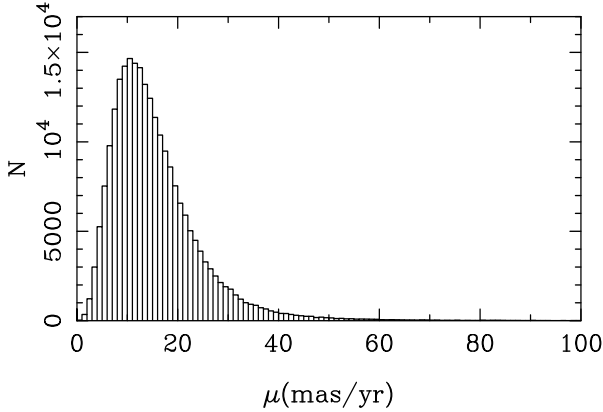


Figure 4. Proper motion frequency distribution

that fainter objects also have more uncertain proper motion determinations. The peak of the proper motion distribution therefore moves to higher proper motions with object samples drawn from progressively fainter magnitude bins. For this reason, we consider the survey proper motion limit as a function of magnitude.

Three independent methods of determining an appropriate proper motion limit have been investigated for this dataset:

- (1) analysis of proper motion error distribution
- (2) cumulative proper motion number counts
- (3) RPMD inspection

all of which are described here.

The characteristics of the ‘noise’ in the proper motion distribution can be analysed by assuming all objects are ‘zero proper motion objects’ and the calculated proper motions arise purely from random measurement error. The ‘true’ values of μ_x and μ_y measured by linear regression are therefore zero, and the random measurement errors give rise to a normal error distribution in μ_x and μ_y about zero with common σ . We are of course interested in the total proper motion, which follows a Rayleigh distribution of the form

$$P(\mu) = \frac{\mu}{\sigma^2} e^{-\frac{\mu^2}{2\sigma^2}}. \quad (1)$$

This survey utilises two independent measures of proper motion in the same field, one from the stacks of B plates and the other from the R stacks. A useful means of reducing the final proper motion survey limit will be to compare these two measures and reject inconsistent motions. Comparison of independent measures of proper motion needs to be incorporated into this analysis if it is to be useful in predicting sample contamination later. The measured B and R motions and their associated error distributions are therefore characterised

$$P(\mu_b) = A_b \mu_b e^{-C_b \mu_b^2} \quad (2)$$

and

$$P(\mu_r) = A_r \mu_r e^{-C_r \mu_r^2} \quad (3)$$

respectively. The algorithm used to select sample objects on

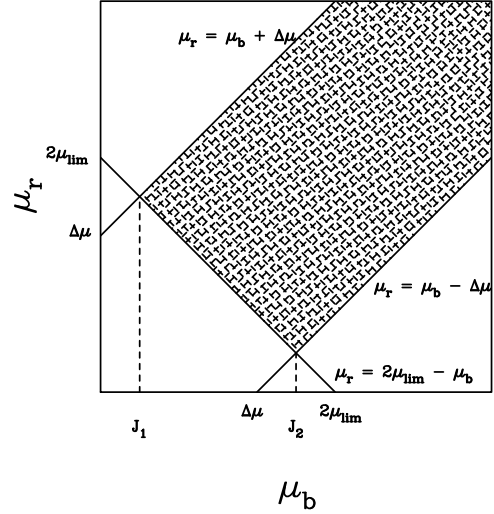


Figure 5. Objects will only be selected for the survey sample if their proper motions lie in the hatched region of the diagram.

the basis of proper motions will use three sequential cuts to eliminate spurious motions. Firstly, the averaged proper motion must exceed the proper motion limit μ_{lim} , ie:

$$\frac{\mu_r + \mu_b}{2} > \mu_{lim}. \quad (4)$$

Secondly, the difference in proper motion must not exceed a second survey parameter ($\Delta\mu$):

$$|\mu_b - \mu_r| < (\Delta\mu), \quad (5)$$

and finally the difference in position angle must not exceed a third survey parameter ($\Delta\phi$):

$$|\phi_j - \phi_r| < (\Delta\phi). \quad (6)$$

An object must satisfy all three of these criteria to be included in the sample. The desired outcome of this analysis is the ability to predict the expected contamination from spurious motions for a survey with parameters μ_{lim} , ($\Delta\mu$) and ($\Delta\phi$) given the ‘zero proper motion object’ error distribution described by equations 2 and 3. In order to do this we consider the combined probability distribution $P(\mu_b)P(\mu_r)$ on the $\mu_b - \mu_r$ plane. The survey criteria described above effectively limit the selected sample to a specific area on the $\mu_b - \mu_r$ plane, shown in Figure 5. Given a realistic estimate of the (normalised) $P(\mu_b)$ and $P(\mu_r)$ distributions an integration over the hatched region in Figure 5 yields an estimate for the fraction of objects, X , belonging to the error distribution likely to contaminate the sample. The integral

$$X = \int_{J_1}^{J_2} \int_{2\mu_{lim} - \mu_b}^{\mu_b + (\Delta\mu)} P(\mu_b)P(\mu_r) d\mu_r d\mu_b + \int_{J_2}^{\infty} \int_{2\mu_b - (\Delta\mu)}^{\mu_b + (\Delta\mu)} P(\mu_b)P(\mu_r) d\mu_r d\mu_b \quad (7)$$

where

$$J_1 = \frac{2\mu_{lim} - (\Delta\mu)}{2} \quad (8)$$

and

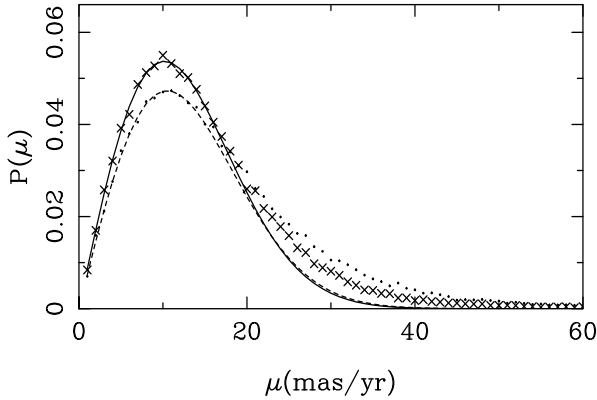


Figure 6. Normalised B (dashed line and dots) and R (solid line and crosses) measured data (points) and fitted error distributions (lines). This example uses the first 15 data points to determine the error distribution.

$$J_2 = \frac{2\mu_{lim} + (\Delta\mu)}{2} \quad (9)$$

is easily calculated numerically for arbitrary μ_{lim} and $(\Delta\mu)$. Since this analysis concerns zero proper motion objects whose spurious motion arises purely from machine measurement error, we may assume no preferred position angle, and the resulting fraction X will be cut by a further $(2(\Delta\phi))/360$ ($(\Delta\phi)$ in degrees) by the position angle selection criterion, ie.

$$X_{final} = \frac{X}{2(\Delta\phi)/360}. \quad (10)$$

The calculation described above requires knowledge of the $P(\mu_b)$ and $P(\mu_r)$ ‘zero proper motion’ error distributions. If equation 7 is to be used to calculate numbers of contaminants it is important that $P(\mu_b)$ and $P(\mu_r)$ can be simultaneously rescaled from normalised distributions. The B and R data are therefore paired so that $P(\mu_b)$ and $P(\mu_r)$ contain the same objects and thus the same number of objects. For the purposes of this analysis this proper motion data is thought of as consisting of two distinct distributions: the ‘zero proper motion object’ error distribution, on which a distribution of real proper motions is superposed. Any attempt to determine the error distribution from the measured distribution must use only the low proper motion data where the random errors of interest dominate systematics introduced by real proper motions. In the example to be shown here the first 15 bins (1mas/yr bins) of the normalised proper motion distribution is taken to be representative of the error distribution.

The first 15 data points in both B and R are fitted with an assumed error distribution like equation 3. These fits are shown along with the measured data in Figure 6, with the real data rising above the error fits representing real proper motions. Since the error distributions exclude real motions they must be renormalised before use in equation 7. The rescaling factor to be used in calculating numbers of contaminants is taken to be the number of objects contained in the error distributions. This number will in general be different for the B and R data, so the average is used. Nu-

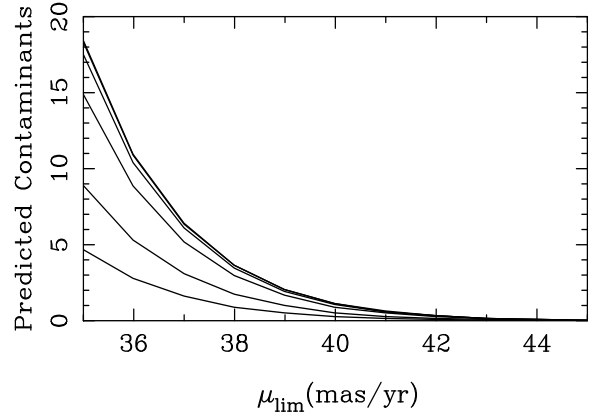


Figure 7. The results of numerical integration predicting the number of contaminant objects in the survey sample as a function of survey proper motion limit. The lower of the lines used a $(\Delta\mu)$ of 5 mas/yr, with $(\Delta\mu)$ rising to 50 mas/yr for the top line ($(\Delta\phi)$ was set to 90 throughout). These calculations were based on error distributions determined from the first 15 proper motion bins of the measured μ_b and μ_r distributions.

merical methods can now be used to predict the number of contaminant spurious proper motions for a range of μ_{lim} , $(\Delta\mu)$ and $(\Delta\phi)$ using equations 7 and 10. The result of a series of calculations is shown in Figure 7. The predicted contamination falls rapidly below one object as μ_{lim} exceeds ~ 42 mas/yr. Care must be taken however that the error distributions are not overly sensitive to the number of points in the measured μ_b and μ_r distributions used in their calculation. The error distributions were therefore recalculated using the first 30 bins in the measured μ_b and μ_r distribution and the predicted contamination plot redrawn using these new distributions. The two calculations prediction of the μ_{lim} at which the survey contamination drops to below 1 object are consistent to within ~ 3 mas/yr. Presented in Table 2 are the results of calculating the μ_{lim} at which the predicted number of contaminant objects falls below one for a range of magnitude cuts, $(\Delta\mu)$ and derived $P(\mu_b)$, $P(\mu_r)$ distributions. Table 2 indicates that the $(\Delta\mu)$ survey parameter has a small bearing on the μ_{lim} where $N_{contam} \sim 1$. The $(\Delta\mu)$ criterion can therefore be relaxed substantially to ensure no real motions are rejected. A similar argument is applicable to the $(\Delta\phi)$ parameter, where the small advantage gained by tightening the $(\Delta\phi)$ criterion again becomes increasingly outweighed by the potential for rejection of real proper motions. To conclude comment on this analysis, any μ_{lim} greater than ~ 45 mas/yr should eliminate contamination arising from normally distributed positional measurement errors, although thus far no account has been taken of spurious motions arising from other sources (eg. erroneous pairings).

The second means of investigating the proper motion limit is via proper motion number counts. Assuming the local Disc has constant stellar density and that Disc kinematics give rise to an approximate inverse correlation between distance and proper motion, a plot of log cumulative number count (from large to small μ) versus log μ should fol-

R magnitude cut	No. of μ_b, μ_r data points used	μ_{lim} (mas/yr) for varying $(\Delta\mu)$			
		$(\Delta\mu)=5$	$(\Delta\mu)=10$	$(\Delta\mu)=30$	$(\Delta\mu)=50$
$R > 20.5$	15	40	41	42	43
	25	41	43	44	44
$20.5 > R > 20$	15	34	35	36	36
	25	34	35	36	36
$20 > R > 17$	15	30	31	32	32
	22	32	33	33	33
$R < 17$	15	31	32	33	33
	25	34	35	36	36

Table 2. Calculated μ_{lim} where predicted number of contaminants falls below 1 object. Column two represents the number of bins in the measured μ_b and μ_r distributions used to derive the $P(\mu_b), P(\mu_r)$ distributions.

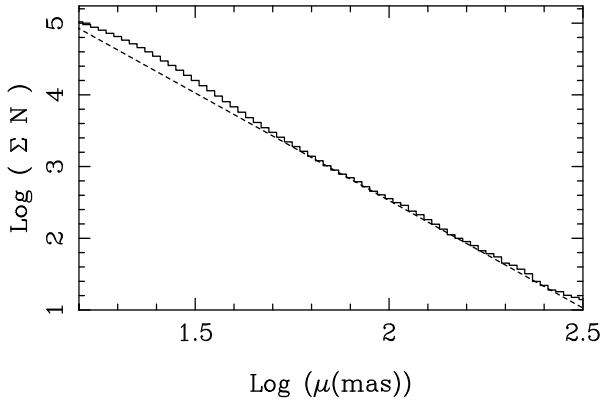


Figure 8. Cumulative number counts plot showing deviation from simple model at $\mu \sim 50 \text{ mas/yr}$.

low a straight line of gradient -3 (ie. $\log \sum N \propto -3 \log \mu$). In principle a proper motion limit for this survey could be obtained by determining the point at which our measured proper motions deviate from this relation due to the existence of spurious motions. In Figure 8 the cumulative number counts are plotted as a histogram. If the points between $\log \mu = 1.9$ and $\log \mu = 2.5$ are fit with a straight line the resulting gradient is (-2.998 ± 0.071) , in excellent agreement with the idealised predicted slope of -3 . The fit is shown as a dashed line. This finding compares favourably with a similar analysis of Luyten (1969, 1974, 1979) and Giclas (1971, 1978) common proper motion binary stars, which on an analogous plot describe a straight line of significantly shallower gradient than the expected -3 indicating increasing incompleteness with decreasing proper motion (Oswalt & Smith 1995). Towards lower proper motions our data rises above the line, indicating the onset of contamination at $\mu \sim 50 \text{ mas/yr}$, lending credence to the findings of the previous analysis.

The final means of assessing the effects of varying μ_{lim} is the RPMD. The RPMD is, for all sample objects lacking follow up observations, the sole means of stellar population discrimination. For this reason it is worthwhile inspecting the RPMD of samples produced using various survey limits. The principal concern is that the white dwarf locus be

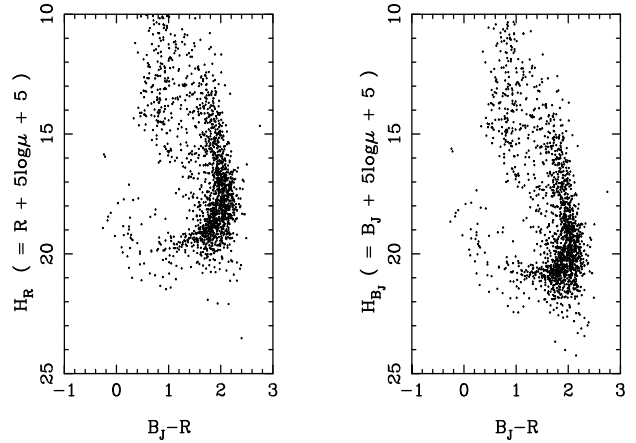


Figure 9. A RPMD of a sample with $\mu_{lim} = 50 \text{ mas/yr}$ for all objects.

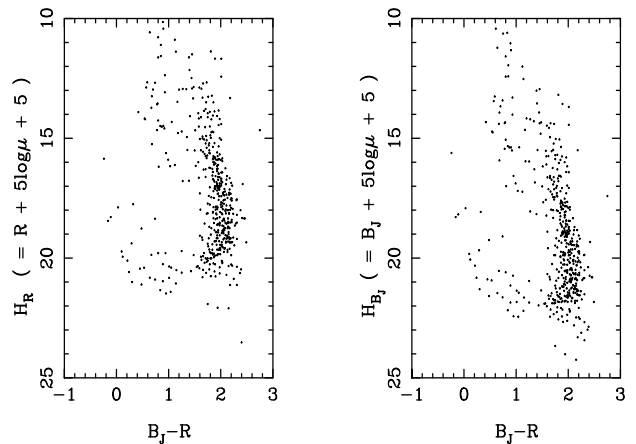


Figure 10. A RPMD of a sample with $\mu_{lim} = 80 \text{ mas/yr}$ for all objects.

as distinct as possible at all colours while maximising the sample size.

It can be argued that there is little purpose in lowering μ_{lim} for bright objects to anything near the level of potential contamination. Consider searching for an intrinsic

cally faint star such as a reasonably cool white dwarf, with an absolute R magnitude of ~ 14 , amongst survey objects with apparent R magnitudes as faint as ~ 19 . Such an object, having a (conservative) tangential velocity of 40km/s, would have a proper motion of $\sim 80\text{mas/yr}$ – well beyond the predicted contamination limit. This argument becomes even more forceful for both intrinsically fainter and apparently brighter objects, implying that a conservative μ_{lim} is desirable for all but the faintest survey objects.

Figure 9 is a RPMD produced with a μ_{lim} of 50 mas/yr at every magnitude. The main sequence and white dwarf loci are visible, as is a dense group of objects between the two at $H_R \sim 19.5$. This group of objects probably consists of two sub-groups. Firstly of course, the most likely sample contaminants are faint objects creeping through just over the proper motion limit at this point. Secondly, one would expect a large population of objects to lie on the RPMD where the μ and R distributions are most populated, ie. at μ_{lim} and at faint R (an object with $\mu = 50\text{ mas/yr}$ and $R=21$ has $H_R = 19.5$), and it should therefore not be automatically assumed that every object lying at this point in the RPMD is suspect. A cause for concern however, is the way this population bridges the gap between the main sequence and the white dwarf population, a property one would expect from a contaminant locus rather than the detection of bona fide proper motions. If a more conservative limit of $\mu_{lim}=60\text{ mas/yr}$ is adopted for objects with $R > 20.5$ the RPMD (Figure 11) looks more promising, with the ‘contaminant locus’ all but gone, leaving only the expected mild confusion (Evans 1992) between populations at their faint extremity. The adoption of an extremely conservative μ_{lim} of 80 mas/yr for all objects leads to an even more well defined RPMD (Figure 10), where the white dwarf population discrimination is almost without exception unambiguous.

The survey parameters to be used to select the preliminary sample (ie. a sample subject to further object-by-object scrutiny and potential rejection, with the possibility of further objects being included the sample which lie just outside the RPM cut on one or both RPMDs) have been chosen with reference to the findings in this section.

Error analysis and number counts suggest a μ_{lim} of 50 mas/yr, a $(\Delta\mu)$ of 50 mas/yr and a $(\Delta\phi)$ of 90 degrees should essentially eliminate contamination arising from normally distributed measurement errors. It was found, however, that the white dwarf locus is insufficiently distinct in the RPMD obtained using these survey parameters. A slight restriction of μ_{lim} for objects with $R \geq 20.5$ does much to solve the population discrimination problem. Therefore the survey parameters given above, with the exception of a μ_{lim} of 60 mas/yr for object with $R \geq 20.5$, appears to be an acceptable compromise between sample maximisation and potential contamination and population discrimination problems.

The RPM can be expressed in terms of tangential velocity, V_T , and absolute magnitude, M :

$$H = M + 5 \log_{10} V_T - 3.379. \quad (11)$$

Evans (1992) has produced theoretical RPMDs by using expected $5 \log_{10} V_T$ distributions and absolute magnitude - colour relations for various populations. Although these theoretical predictions were made for specific fields and incorporated error estimates peculiar to that work, they serve

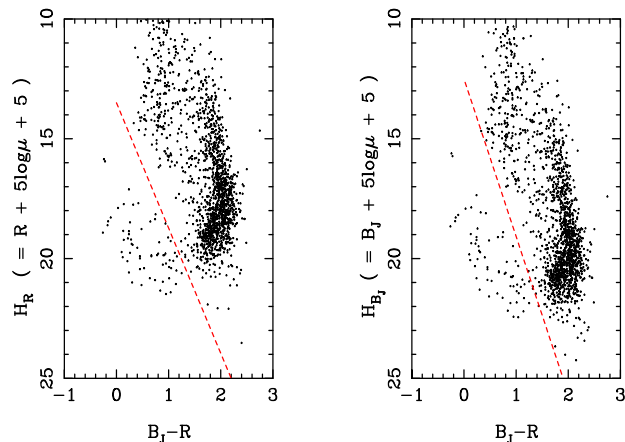


Figure 11. RPMD of the survey sample showing the white dwarf population divider used.

as a useful guide to the expected distribution of stellar populations on the RPMD. The RPMD white dwarf population locus is found to be an unambiguous population discriminator for all colours blue-wards of $(O - E) \sim 1.8$, with an increasing chance of contamination from the spheroidal main sequence population red-wards of this colour. Transforming from $(O - R)$ to $(B - R)$ (Evans, 1989 - equation 13), spheroidal population contamination should become a problem red-wards of $(B - R) \sim 1.6$ which in turn corresponds to $(B_J - R) \sim 1.2$. Indeed on inspection of Figure 11, the white dwarf locus does begin to become confused at this colour. This contamination occurs solely from the direction of small RPM, and the RPMD can still be used with some confidence as a population discriminator for objects with high measured RPM red-wards of $(B_J - R) \sim 1.2$. In order to accommodate these contamination considerations, the preliminary survey white dwarf sample is defined as those objects blue-wards (in both plots) of the lines in Figure 11. The lines cut the top of the white dwarf locus at $(B_J - R) \sim 1.2$ but allow slightly redder objects with higher RPMs into the sample. The white dwarf locus is unambiguous blue-wards of $(B_J - R) \sim 1.2$.

Every object in the sample must appear in at least 15 stacks in each passband. The positional data as a function of time have been scrutinised for every object selected as a white dwarf candidate, and those with dubious motions rejected. While such a process may seem rather arbitrary, it was necessary to incorporate this screening stage in the sample extraction because simple automated rejection algorithms such as the 3σ rejection routine used here cannot be guaranteed to eliminate spurious motions. Some examples are shown in Figures 12 and 13. All three objects shown successfully satisfied all the survey criteria. The object plotted at the top of Figures 12 and 13 (KX27) shows a clear, genuine motion in both x and y in both passbands and was included in the final sample without hesitation. The middle object (KX18) has larger positional uncertainties and a smaller overall motion, but still shows consistent, smooth motions and was also included. The final object shows evidence of large non-linear deviations in the last four epochs of the x measures in both passbands. Although the bad-point rejection algorithm has removed at least one datum from

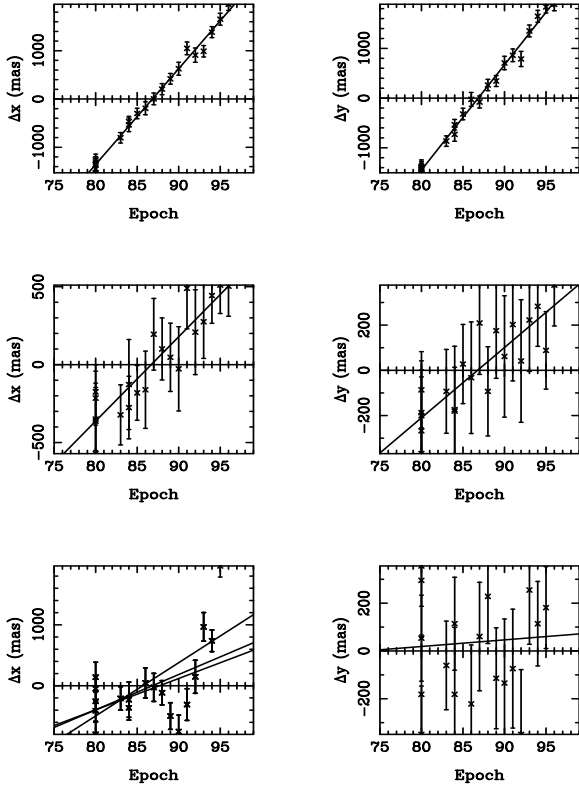


Figure 12. Some example proper motion plots from the R plate stacks. The top plot shows data for object KX27, the middle for KX18 and the lower for a rejected object

each x plot (as shown by the multiple straight line fits), this object shows no evidence of proper motion based on the first 16 data points and certainly cannot be considered a reliable proper motion object candidate. This object, along with 9 others, were rejected from the final WD sample. These rejected objects tended either to have large offsets from a positional distribution otherwise consistent with zero motion at either the first or last few epochs, as is the case with the rejected object described above; or the positional measures had an unusually large scatter around the mean position, indicating the error in position was larger than the objects magnitude would suggest. The reasons for these larger errors may be unusual image morphology or the effect of proximity to a neighbouring object. While this final rejection procedure is unsatisfactory in terms of its lack of objectivity, it is certainly preferable to inclusion of such objects in the final sample, or the introduction of extremely stringent survey limits which would doubtless exclude genuinely interesting objects. The digitised images have also been inspected.

The final sample consists of 56 objects which fully satisfy the photometric, proper motion and RPM/colour survey limits. A further two objects, which satisfy the photometric and proper motion limits but fall marginally outside the RPM/colour cut shown in Figure 11 have also been included after favourable follow up observations detailed in Section 5.

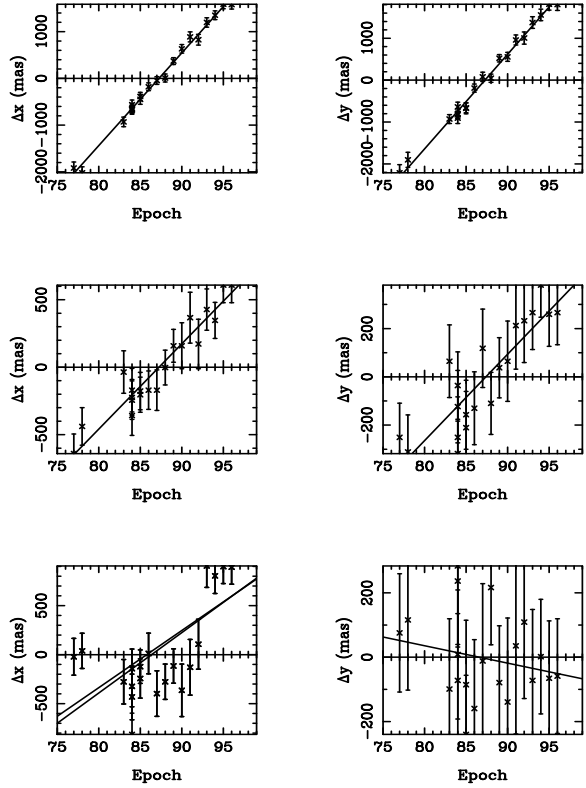


Figure 13. Proper motion plots complementary to Figure 12 from the B_j plate stack data

4 VERY HIGH PROPER MOTION, FAINT OBJECT SENSITIVITY LIMITS

In the previous Section, we discussed in some detail the checks made to establish a clean astrometric and photometric catalogue. The availability of plates over such a wide epoch range as detailed in Table 1 allowed us to search for faint and/or very high proper motion objects in this field. This is important for a number of reasons. For example, it is crucial to firmly establish what the upper limit of detectable proper motion is for the methods used, and also to check if significant numbers of objects have been missed because of this limit or because of the pairing algorithm used. Also, it is important to check at fainter magnitudes for very dim, high proper motion objects since it is the coolest (and therefore faintest) objects that constrain the age determination based on the turn-over in the WDLF. It is also interesting to search for very faint, high proper motion halo WDs in the light of the current debate concerning the origin of the dark lensing bodies detected in microlensing experiments (eg. Isern et al. 1998 and references therein).

We performed three experiments to investigate high proper motion and/or faint objects:

- (i) Within the restricted epoch range 1992 to 1996, ie. five separate epochs, each consisting of a stack of four R plates, we used completely independent software employing a ‘multiple-pass’ pairing technique aimed specifically at detecting high proper motion objects. This software has successfully detected a very cool, high proper motion degenerate WD 0346+246 elsewhere (Hambly, Smartt & Hodgkin 1997). The pairing algorithm described previously used a 200 μ m

search radius over 19 yr resulting in an upper limit of ~ 1 arcsec yr^{-1} , whereas in the multiple-pass test we used a maximum search radius of $650\mu\text{m}$ over a 4 yr baseline, theoretically enabling detection of objects with annual motions as high as ~ 10 arcsec. The highest proper motion object detected in the catalogue was relatively bright ($R \sim 14$), with $\mu \sim 0.8$ arcsec yr^{-1} . This experiment revealed two $\mu \sim 0.8$ arcsec yr^{-1} objects, the one mentioned above and another slightly fainter object ($R \sim 15$); no objects were found with motions larger than this. The colours and reduced proper motions of the two objects indicate that they are M-type dwarfs. The second object was undetected in the catalogue due to a spurious pairing, an increasingly likely scenario for high proper motion objects detected without a multiple pass algorithm since they move substantially from their master frame position. We note that all the expected objects having $\mu > 0.2$ arcsec yr^{-1} detected in the catalogue were also found by this procedure.

(ii) Using the procedure described in the previous Section, but with a relaxed minimum number of epochs, high proper motion objects were searched for. With a $200\mu\text{m}$ pairing requirement over a maximum epoch separation of 7 yr, the upper limit of proper motion was ~ 1.9 arcsec yr^{-1} . The two objects having $\mu \sim 0.8$ arcsec yr^{-1} found in the previous experiment were also recovered here; again, no objects were found with motions larger than this.

(iii) To investigate the possibility of fainter objects, we stacked up the R band material in groups of 16 plates at epochs 1980, 1983 to 1986, 1987 to 1991 and 1992 to 1996. Obviously, over any individual four year period an object having a proper motion greater than ~ 1 arcsec yr^{-1} will have an extended image and will not be detected to the same level of faintness as a stationary star; nonetheless, the $\sim 0.75^{\text{m}}$ increase in depth afforded by going from 4 to 16 plate stacks (eg. Knox et al. 1998) at least allows us to investigate the possible existence of objects having $\mu \sim 0.5$ arcsec yr^{-1} down to $R \sim 23$ (100% complete to $R \sim 22$) over an area of 25 square degrees. In this experiment, all the objects expected from the catalogue were recovered; in addition, one star was found having $R \sim 20$, $\mu = 0.47$ arcsec yr^{-1} at $\text{PA} = 179^\circ$ and $\text{RA,DEC} = 21\text{h}30\text{m}8.553\text{s}$, $-44^\circ 46' 24.09$ (J2000.0). This object is the M-type dwarf ‘M20’ discovered in the photometric survey of Hawkins & Bessell (1988) and has $B_J \sim 23$. The faintness in the blue passband is the reason that this object is absent from the catalogue. Once more, no other high proper motion, fainter stars were found.

These three experiments allow us to be confident that there is no large population of objects having $\mu \gtrsim 1$ arcsec yr^{-1} down to faintness limits of $R \sim 22$ and $B_J \sim 23$. Furthermore, the cut-off in the WD sequence seen in the reduced proper motion diagrams is real, and not an artefact of incompleteness.

5 FOLLOW UP OBSERVATIONS

While the RPMD technique is a powerful population discriminator, it is desirable to obtain follow up observations of a sub-set of sample members. The principle motivation for this is to explicitly demonstrate the applicability of our survey technique by confirming the WD status of the sample objects via spectroscopy. Spectroscopic observations red-

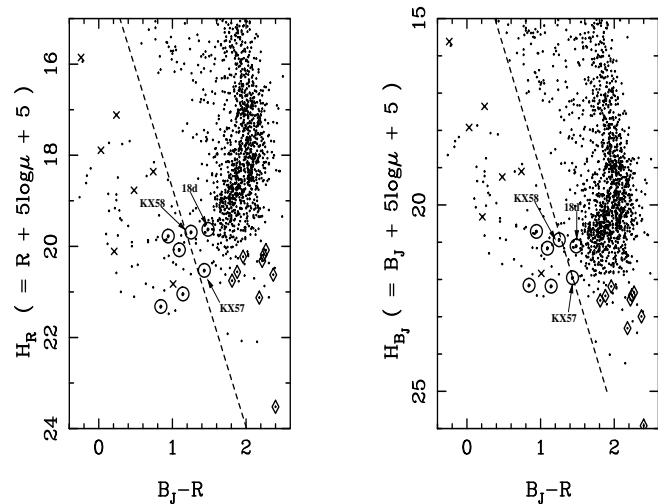


Figure 14. RPMD of the survey sample with spectroscopically observed objects numbered and highlighted. Diamonds denote objects identified as subdwarfs or M dwarfs, crosses an immediate firm WD identification. Dotted circles represent objects with ambiguous spectra (see text). The labelled objects have their spectra discussed in detail below.

wards of the WD cut in the RPMD may also be used to investigate the possibility of ultra-cool white dwarfs existing in the sample; and as a corollary to this, such observations allow clearer population delineation in the RPMD. In addition, photometric observations through standard filters ensure confidence in photographic-to-standard photometry transformations, provide useful independent checks of stellar parameters (eg T_{eff}) derived from fits to photometry and may in future allow alternative population discrimination via eg. colour-colour plots.

5.1 Spectroscopy

This project was allocated 3 nights of observing time in 1996 between the 8th and 10th of August, and a further 3 nights in 1997 between the 5th and 7th of August on the 3.9m Anglo-Australian Telescope. A spectral coverage of 4000-7500Å was obtained with the RGO spectrograph and 300B grating in conjunction with the Tek CCD. Various standards were observed throughout each usable night and CuAr lamp exposures used for wavelength calibration. The data were reduced following standard procedures within the IRAF * environment.

The strategy behind these observations was to define as clearly as possible the constituents of the lower portion of the RPMD, from the blue end of the WD locus down to the extremely high H objects below the M stars. The spectroscopically observed proper motion sample objects are shown in

* IRAF is distributed by the National Optical Astronomy Observatories, which is operated by the Association of Universities for Research in Astronomy Inc., under contract with the National Science Foundation of the United States of America.

Figure 14. Both the unambiguous bluer region of the WD locus and the portion of RPMD lying red-ward of our WD cut generally consist of fairly bright objects. These regions have been probed spectroscopically, albeit more sparsely than the cool WD region consisting of mostly very faint objects. A combination of poor weather conditions at the AAT and the faintness of our CWD sample has rendered high signal-to-noise spectra of these objects unobtainable thus far.

The bluest objects have clearly defined Hydrogen Balmer lines with equivalent widths equal to or in excess of those typical for DA white dwarfs of similar colour (Greenstein and Liebert, 1990). The objects red-wards of our sample cut below the main sequence (MS) show spectra clearly distinct from cool WDs. Both subdwarfs and high velocity M dwarfs have been identified in this region of the RPMD.

A star lying near the cut-off region of the RPMD clearly showing the absence of strong metal features that would be present even in a low-metallicity subdwarf is very likely a CWD. We apply this line of argument to our data by selecting from the recent models of Hauschildt et al. (1998) a spectrum appropriate to a subdwarf (metallicity $[M/H] \geq -2$) of similar effective temperature to a given CWD sample object spectrum. The model spectrum is smoothed to the approximate resolution of the AAT spectra and multiplied through by a synthetic noise spectrum commensurate with the AAT CWD spectrum in question. The only features likely to be visible after this procedure are $\sim 5200\text{\AA}$ MgI and the $\sim 4300\text{\AA}$ CH G-band, and it is in these regions that we look for any evidence that our CWD sample objects are in fact subdwarfs.

This procedure has been undertaken for all CWD candidate spectra. Of these, the spectra of the three objects lying within the region of serious potential subdwarf contamination are displayed, and we restrict comment on the investigation of the bluer objects to the statement that none show any evidence of subdwarf like spectral features. KX58, displayed in Figure 15, is a convincing CWD candidate, showing a smooth continuum spectrum with no suggestion of the metal features apparent in the model subdwarf spectra. The noisier spectrum of KX57 in Figure 16 also shows no evidence of subdwarf features, although poorer signal-to-noise makes the identification less certain. The object 18d lies significantly red-ward of our CWD cut-off on the RPMD, and unfortunately its spectrum (Figure 17) is extremely noisy. While it is difficult to draw any conclusions from such poor data, the dip at $\sim 5200\text{\AA}$ is a reasonable indication that this object is a subdwarf or MS star. Thus the position of 18d on the RPMD in conjunction with the spectral data evidence means this object does not warrant inclusion in our CWD sample.

To summarise the findings of our spectroscopic survey, the only objects showing notable deviation from expected WD spectra are the objects below the M dwarf portion of the RPMD (diamonds in Figure 14) and the more ambiguous case of object 18d discussed above.

5.2 Photometry

CCD photometry of a subsample of our CWD sample was obtained between 29th of July and the 4th of August 1997 on the 1m telescope of the South African Astronomical Observatory in Sutherland. Johnson-Cousins V, R, I pho-

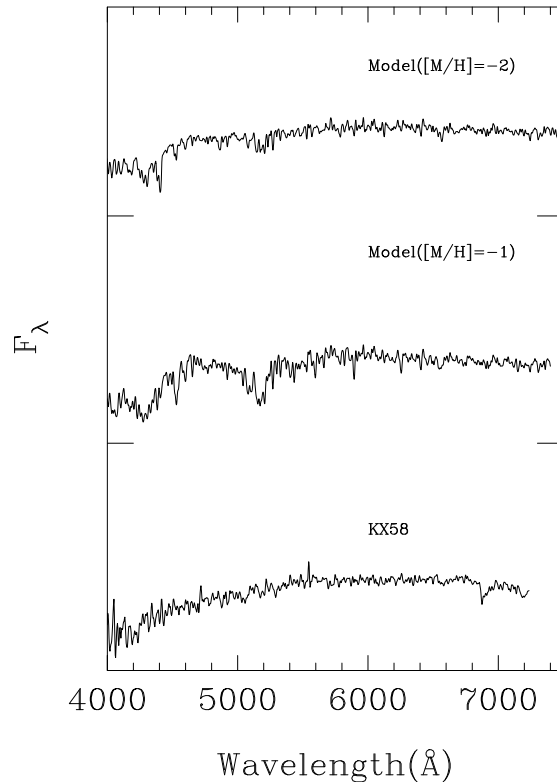


Figure 15. Spectrum of KX58 with comparison model subdwarf spectra

tometry was obtained for all program stars on the Tek (512x512) CCD, with B measures also acquired for sufficiently bright objects. E-region standards were observed continuously through each usable night. Observed magnitudes with associated errors are displayed in Table 3.

These observed magnitudes provide an independent check on the accuracy of the SuperCOSMOS photographic photometry, and we use the deviations of $m_{\text{photographic}}$ from m_{CCD} to obtain errors on the B, V, R, I photographic photometry of 0.17, 0.14, 0.13 and 0.16 respectively. The CCD photometry also allowed tighter estimates of effective temperature to be derived for observed objects, although they did not provide the hoped for useful constraints on $\log g$.

6 SAMPLE ANALYSIS

Previous studies of CWD samples (eg LDM, BRL) have often benefited from a comprehensive and wide ranging observational database, including high quality spectra, optical and IR photometry and parallaxes. These observations, in conjunction with detailed WD models, allow determinations of stellar parameters such as effective temperature, $\log g$, atmospheric composition, mass and bolometric luminosity. However, since this is a relatively new project and is concerned with stars of unusually faint apparent magnitude, such a database does not yet exist for this sample. It is therefore necessary for us to restrict our analysis, in the

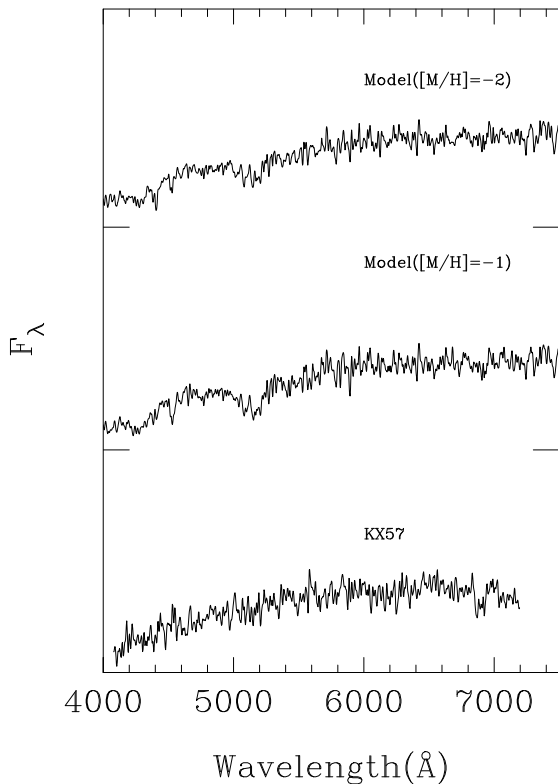


Figure 16. Spectrum of KX57 with comparison model subdwarf spectra

first place by exploiting the homogeneity of WD masses by assuming a common typical $\log g$ for our entire CWD sample (the 60 stars with measured $\log g$ in BRL have a mean surface gravity $\log g = 8.099 \pm 0.044$), and secondly by treating the atmospheric constituent of each star as an unknown parameter whose influence on the resulting WDLF must be determined later.

Bergeron et al. (1995) have published a detailed grid of model predictions for Johnson-Cousins U, B, V, R, I (and IR) photometry and bolometric corrections as a function of effective temperature and $\log g$. Making our assumption that $\log g$ is always equal to 8, values for effective temperature and bolometric luminosity assuming both a H and He atmosphere can be calculated for every sample object.

Fitting for T_{eff} is achieved by interpolating the model grid at 10K intervals for the colour indices $(U - B)$, $(B - R)$, $(V - R)$ and $(V - I)$. We then evaluate χ^2 at each T_{eff} interval using all available colour indices for the object in question. While the photographic photometry is effective in adequately constraining T_{eff} , smaller errors are obtainable with the SAAO CCD photometry, and it is used where available. The resulting χ^2 , T_{eff} distribution yields a fitted value for T_{eff} and an estimate of the associated error, which can be used to read off interpolated values of absolute V magnitude and bolometric luminosity. This procedure is performed for each object for both an assumed H and He atmosphere.

Distance moduli obtained from these fits allow calculation of tangential velocities via the SuperCOSMOS proper

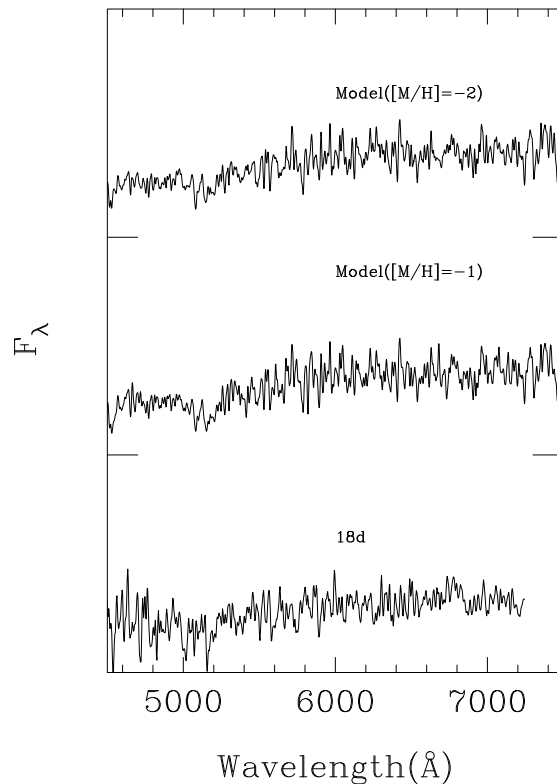


Figure 17. Spectrum of 18d with comparison model subdwarf spectra

motion measures. The distribution of derived tangential velocities is consistent with expectations for a sample of Disc stars (Evans 1992), and shows no evidence of contamination from high velocity halo objects. A summary of the results of the fitting procedure is shown in Table 4, including T_{eff} and M_{bol} with associated errors and V_{tan} values. Space density values for each object are also presented in Table 4; these are discussed in the following section.

An independent check on the validity of our initial CWD sample parameters (SuperCOSMOS photometry and astrometry) can be made by comparing known CWD samples with our data on the RPMD. Since the RPMD is the original means of population discrimination it is also interesting to overplot known subdwarf samples on our RPMD to further address the question of potential contamination. BRL published observations of a sample of 110 CWDs, including most of the coolest known degenerates. Extensive lists of extreme subdwarfs are less easily obtainable. Ryan (1989) used a RPM criterion to extract over 1000 subdwarf candidates from the NLTT catalogue. Accurate B and R photometry was published for these objects, providing a useful means of delineating the bluer portion of the WD RPMD locus. Monet et al. (1992) identified a subset of 17 extreme subdwarfs from their CCD parallax program also involving Luyten catalogue stars. Although only V, I photometry is published for these stars, we use the photometry published in Ryan (1989) to define colour transformations allowing the 17 subdwarfs from Monet et al. (1992) to be plotted on

Object	B	V	R	I
	σ_B	σ_V	σ_R	σ_I
KX14(1)	–	21.43	20.78	20.17
		0.04	0.09	0.07
KX14(2)	–	21.47	20.75	20.20
		0.04	0.07	0.07
KX15	19.10	18.53	18.08	17.69
	0.03	0.02	0.03	0.03
KX20	16.14	16.12	16.16	16.22
	0.02	0.02	0.02	0.02
KX22	–	19.94	19.66	19.55
		0.03	0.04	0.04
KX23	19.52	19.05	18.74	18.61
	0.03	0.01	0.01	0.03
KX27	–	18.15	17.97	17.91
		0.02	0.02	0.03
KX29	18.67	18.36	18.17	17.90
	0.03	0.02	0.03	0.03
KX30	–	21.12	20.64	20.19
		0.03	0.05	0.08
KX33	–	21.22	20.69	20.10
		0.04	0.06	0.07
KX39	–	21.19	20.66	20.18
		0.04	0.06	0.06
KX41a	20.26	19.38	18.93	18.41
	0.05	0.03	0.04	0.04
KX41b	20.28	19.33	18.81	18.36
	0.04	0.03	0.04	0.04
KX44	–	21.37	20.81	20.42
		0.05	0.07	0.08
KX53	–	20.96	20.70	20.21
		0.03	0.05	0.06
KX57	–	21.09	20.40	19.84
		0.04	0.06	0.08

Table 3. Johnson-Cousins CCD photometry taken at SAAO for selected members of our CWD sample. Object KX41 was resolved as a double-degenerate on the CCD frame and thus has photometry for each component. Object KX14 had two independent sets of observations, shown as (1) and (2)

the $(B - R)$, RPMD planes. These objects define a portion of the RPMD marginally red-wards of the faintest CWDs where the most extreme contaminants may be expected to lie.

Figure 18 shows the two RPMD with the four samples plotted. There are several points to be made concerning this plot. Firstly, our CWD sample and the the BRL sample of previously known CWDs lie on the same region of the diagram, providing further confirmation of the validity of our survey procedure. It can also be seen that the BRL sample contains redder, cooler stars than our sample. This may be expected since the BRL sample is rather eclectic and contains some of the coolest WDs known, whereas our sample is drawn from a rigidly defined survey in a particular ESO/SERC field. We note also that the cool portion of the BRL sample does not extend into the portion of the RPMD beyond our population discrimination cut-off shown in Figure 11, which may be interpreted as indicating that we are not failing to sample portions of the RPMD containing CWDs (but see Section 8 below). Both subdwarf samples lie in clearly distinct regions of the RPMD to our sample, although the cooler subdwarfs are all too red to directly

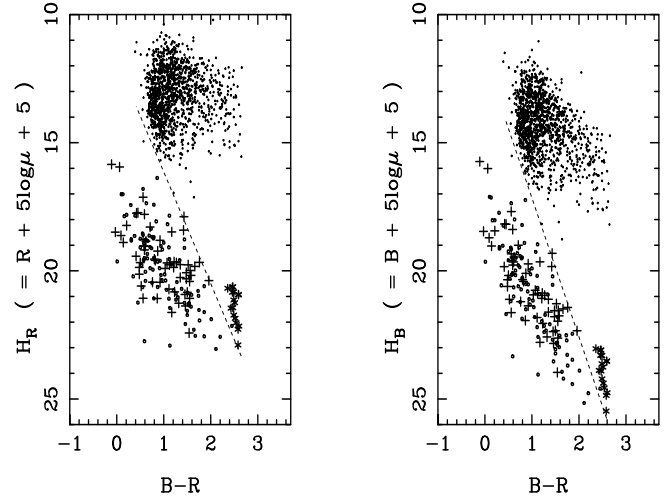


Figure 18. A comparison of various populations on the RPMDs: crosses denote our CWD sample, circles the BRL CWD sample, asterisks the Monnet et al. extreme red subdwarfs and dots the brighter Ryan subdwarfs

assess contamination of the CWD sample from the direction of small RPM. However the subdwarf RPM locus is not predicted to deviate significantly from a straight line in the CWD colour regime (Evans 1992), and if we take the high H extent of the two subdwarf samples plotted to be indicative of the limit of the extreme subdwarf locus on the RPMD, the dashed lines plotted on Figure 18 should be a good guide to the limit of the subdwarf locus for the intermediate colour range. It may then immediately be seen that the vast majority of our CWD sample is safely within the WD region of the RPMD. The two redder borderline stars have reasonable spectroscopic confirmation of their WD status (Figures 16 and 15), leaving only one potentially dubious object.

7 THE WDLF

In order to construct a WDLF, space densities must be calculated for a survey limited by both apparent magnitude and proper motion. The CWD survey sample presented in Table 4 consists of stars with widely varying intrinsic brightness and tangential velocity, and is therefore not volume-limited (since for example intrinsically bright objects are sampled out to greater distances than the coolest, faintest stars). The standard solution to this problem, Schmidt's (1968, 1975) $1/V_{max}$ estimator, has been extensively studied with specific reference to the WDLF (Wood & Oswalt 1998). The $1/V_{max}$ method assigns each sample object a survey volume defined by the maximum distance d_{max} the object could have and satisfy the survey limit criteria. For this survey, an object at distance d with proper motion μ and magnitudes B and R has d_{max}

$$d_{max} = \min \left[d \frac{\mu}{\mu_{lim}}, d 10^{0.2(R_{lim} - R)}, d 10^{0.2(B_{lim} - B)} \right]. \quad (12)$$

For the simple case of uniform stellar space density, the survey field solid angle Ω can then be used to calculate the

corresponding V_{max} ($= \Omega d_{max}^3/3$). However, many of the objects in our CWD sample yield a d_{max} comparable to the scale height of the Disc, and we follow the method of Tinney, Reid & Mould (1993) in generalising our calculation of V_{max} to allow for the truncation of the survey volume by the scale height effect. In this prescription, the volume is found by integrating over an exponentially decreasing density law (Stobie, Ishida & Peacock 1989) with scale height h at galactic latitude b , yielding the modified expression for the volume out to a distance d :

$$V = \Omega \frac{h^3}{\sin^3 b} \{2 - (\xi^2 + 2\xi + 2)e^{-\xi}\}, \quad (13)$$

where $\xi = d \sin b/h$ (Equation 9 in Tinney et al. 1993). Each object is thought of as a sampling of the survey volume V_{max} , and thus contributes a space density of V_{max}^{-1} to its particular LF bin. We adopt the convention of LDM in assigning the uncertainty in each space density contribution as being equal to that contribution (ie. 1 ± 1 objects per sampling). We may therefore construct a LF simply by summing the individual space density contributions in each luminosity bin, and the error obtained by summing the error contributions in quadrature. A true reflection of the LFs observational uncertainties should also allow for the uncertainties inherent in photometric fits to model atmospheres described in the previous section. The errors in M_{bol} detailed in Table 4 suggest the introduction of horizontal error bars in any observational LF is necessary. When converting our sample M_{bol} values into luminosity units via

$$M_{bol} = -2.5 \log L/L_{\odot} + 4.75 \quad (14)$$

we also calculate the upper and lower 1 sigma luminosity uncertainties for each object. For a bin containing N objects we then combine eg. the upper luminosity 1 sigma uncertainties, σ_u , using

$$\sigma_U = \sqrt{\frac{\sum_i^N \sigma_{u_i}^2}{N}} \quad (15)$$

to yield an estimate for the horizontal error bar σ_U , with an analogous procedure for the lower luminosity error bounds. In addition, to give the most realistic estimate for the LF in magnitude bins containing a very few objects, we plot the binned data at the mean luminosity of the objects in the bin, rather than at the mid-point of that bin.

Table 5 gives the LF calculated in this fashion for integer magnitude bins. Only the cool end of the LF is given here ($M_{bol} > 12.25$), and a field size of 0.0086 steradians and Disc scale height of 300 parsecs were used in calculating space densities. Columns 3 and 4 give the plotted (Figure 19) LF with upper and lower error bounds in parenthesis. The hot WD data point not detailed in Table 5 represents the 6 stars with ($3 > -\log L/L_{\odot} > 2$). These hotter objects tend to have large errors in fitted M_{bol} , and the resulting large horizontal error bars makes broader binning appropriate. It is necessary to choose either a pure hydrogen or helium atmosphere for each object to construct the LF. We use our ‘best guess’ atmospheres for the LF described here: for each object we choose the atmosphere with the lower χ^2 model fit to the photometry, with the exception of objects with $6000 > T_{\text{effH}} > 5000$ which are deemed to be occupying the ‘non-DA gap’ at this temperature (BRL) and are therefore automatically designated a pure H atmosphere. Note

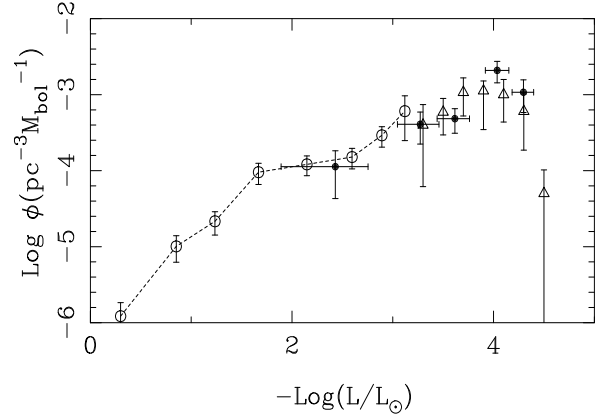


Figure 19. Observational LF with comparisons: this work (filled circles), hot WDLF based on Fleming, Liebert and Green (1986) from LDM (open circles) and the LRB redetermination of the LDM CWDLF (open triangles)

however that the photometry does not adequately constrain atmospheric composition and this ‘best guess’ LF is only one arbitrary realisation of the data (see Section 8 below).

The standard means of assessing the completeness of a sample analysed using the $1/V_{max}$ method is to calculate the mean value of the ratio of V_{obs} , the volume out to an object, to V_{max} . A complete survey evenly sampling the survey volume should yield $\langle V_{obs}/V_{max} \rangle = \frac{1}{2}$. This is generally not the case for published CWD samples, although some authors have incorporated completeness corrections into their analyses to account for the effects of the original survey incompleteness (OSWH). The $\langle V_{obs}/V_{max} \rangle$ calculated for this sample is 0.495 or 0.496 choosing either all H or He atmospheres. From a complete sample containing 58 objects we expect $\langle V_{obs}/V_{max} \rangle = 0.5 \pm 0.038$, indicating our sample is consistent with being drawn from a complete survey. It should be emphasised however that this result cannot be regarded as proof of completeness, since clearly an incomplete survey sample may also exhibit $\langle V_{obs}/V_{max} \rangle \sim \frac{1}{2}$.

The total space density determined from our ‘best guess’ sample is 4.16×10^{-3} WDs per cubic parsec, approximately 25% greater than that found by LRB. These results are certainly consistent, since the simulations of Wood and Oswalt (1998) predict errors of $\sim 50\%$ in total space density estimates from samples of 50 CWDs using the $1/V_{max}$ technique and additional uncertainties are introduced by our lack of knowledge of the WD atmospheric constituents. Our findings reiterate that WDs represent only a small fraction ($\sim 1\%$) of the local dynamically estimated mass density. Interestingly, we do not confirm the much higher total WD space densities found recently by two independent studies. We note however that these studies (Ruiz & Takamiya 1995, Festin 1998) make only a tentative claim to detection of a high WD space density due to the small samples ($N < 10$) involved. A third study (OSWH) searched exclusively for WDs in CPMBs, and found a total space density of 5.3×10^{-3} for these objects. At this space density, and given our survey area and the resolution of the COSMOS data, we would not expect to find any CPMB WDs. It is therefore not surpris-

Bin Center		$-\log L/L_{\odot}$	Space Density $\log \{ [\sum (1/V_{max})] M_{bol}^{-1} \}$	Number
M_{bol}	$-\log L/L_{\odot}$			
12.75	3.20	3.27(3.05,3.45)	-3.39(-3.23,-3.65)	14
13.75	3.60	3.62(3.44,3.76)	-3.32(-3.18,-3.51)	13
14.75	4.00	4.04(3.92,4.15)	-2.68(-2.56,-2.84)	20
15.75	4.40	4.30(4.18,4.40)	-2.97(-2.80,-3.24)	5

Table 5. Luminosity Function

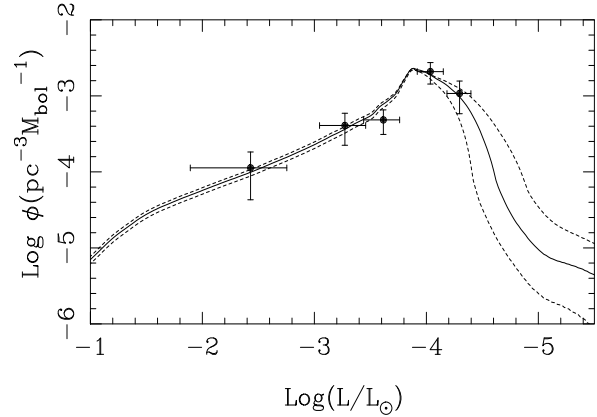
ing that no object in our sample is a CPMB member, since the survey technique is only sensitive to lone WDs or double degenerate binary systems.

8 DISCUSSION

An estimate of the Disc age may be obtained by comparing our WDLF with expectations from theoretical models. We compare our data with two sets of models, which are available in the form of curves at integer 1 Gyr Disc age intervals. Since we are fitting to a cut-off in space density, the *lack* of detected objects beyond our faintest observational bin assumes added significance. We can calculate the probability of detecting zero objects in the next faintest luminosity bin because we have well defined survey limits: at given faint luminosity the proper motion survey limit is irrelevant and the survey is sampling a known volume defined by the photometric survey limits. This volume was calculated using B and R magnitudes for very cool WDs from the recent models of Hansen (1998), which combined with the photometric survey limits yield a d_{max} for both an H and an He atmosphere WD. The minimum d_{max} defines the survey volume at that magnitude. We have assumed the LF at any given luminosity consists of equal numbers of H and He WDs, in which case the H WD survey volume provides the best constraint on the LF and is adopted for fitting. Using Poisson statistics, the probability of detecting zero objects in a volume V in which a model predicts space density ρ is simply $e^{-\rho V}$. We assume the errors on the data points are normally distributed, and derive best fits by maximising the probability of the dataset for each curve and comparing the fits for the various Disc ages.

The various inputs to the first set of WDLFs we use, those of Wood, were described in detail in Wood (1992). Careful consideration was given to the various inputs to the WDLF, such as initial mass function, star formation rates and initial-final mass relation. The Wood WD evolutionary models for the WDLFs have since been updated (Wood 1995, OSWH), and consist of mixed carbon-oxygen core WDs with hydrogen and helium surface layer masses of 10^{-4} and $10^{-2}M_{*}$ respectively, and also utilise revised opacities and neutrino rates. It is these more recent model WDLFs that are used here.

The best fit of our ‘best guess’ LF to the Wood model WDLFs is for a Disc age of 9 Gyr, and is shown in Figure 20. Although this gives a reasonable first indication of the Disc age implied by our sample, further investigation is necessary since the photographic photometry fitting procedure used to estimate T_{eff} (as described in Section 6) does not reliably constrain the atmospheric constituent of the stars in

**Figure 20.** The Wood WDLF with a Disc age of 9 Gyr – the best fit to our ‘best guess’ LF. 8 Gyr (below) and 10 Gyr (above) curves are also shown in dashed lines.

our sample. We have addressed this question by constructing a large number of WDLF ‘realisations’ from our sample data, each time giving each star a 50% probability of having either a H or He atmosphere. Every resulting WDLF was fit to the models and the best fit Disc age recorded. We have also used this analysis to assess the effect of binning on the fitting procedure. Figure 21 (a) displays the results of fits to 1000 realisations binned in 1.0 M_{bol} bins and a further 1000 in 0.75 M_{bol} bins. These results give a fairer indication of the Disc age and associated errors than Figure 20, which is effectively one arbitrarily picked realisation.

The second set of theoretical WDLFs we use are described in García-Berro et al. (1997) (henceforth GB models). These LFs include the expectation that the progenitors of the faintest WDs are likely to have been massive stars since these stars evolve more quickly and the resulting (Oxygen-Neon) massive WDs also cool faster. These models also include a predicted delay in Carbon-Oxygen WD cooling induced by the separation of C and O at crystallization (Hernanz et al. 1994). The incorporation of these considerations into the theoretical WDLF leads to a broader predicted peak at the tail of the LF. We find a best fit of 11 Gyr to our sample, as shown in Figure 22. Again, we have investigated the effect of our poor knowledge of our samples atmospheres in the same way as above. The results, shown in Figure 21 (b), highlight the effect that variations in binning can have on the fits for this second set of models.

The major contributor to this problem seems to be that the model curves are sufficiently indistinct in the region of

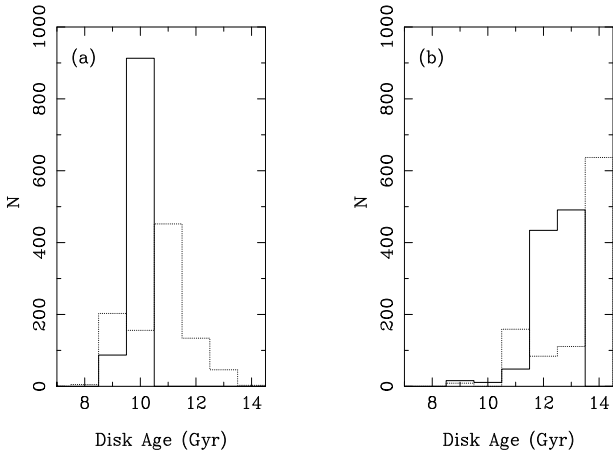


Figure 21. Results of constructing WDLFs from our sample by randomly assigning H or He atmospheres. Full line histograms denote $1 M_{\text{bol}}$ bins, dotted lines $0.75 M_{\text{bol}}$ bins. For each bin size 1000 realisations of the WDLF were constructed and fit to the models - the number of times each Disk age was the best fit is displayed. Graph (a) shows fits to the Wood models, graph (b) fits to GB.

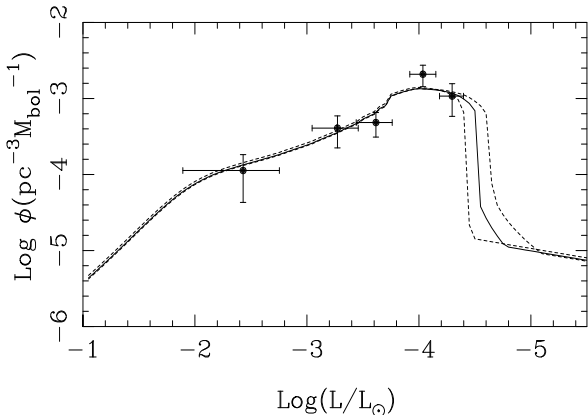


Figure 22. The best fit of our ‘best guess’ LF to the GB WDLF: a Disk age of 11 Gyr with ‘adjacent’ Disk age LFs shown in dashed lines as in Figure 20.

our sample dataset (as can be seen clearly in Figure 22) that changes in observational LF binning can have a significant bearing on the result of the fit. This effect is apparent in Figure 21 (b), where a bin size of $0.75 M_{\text{bol}}$ yields a strong preference of a Disk age of 14 Gyr, in contrast to the 12–13 Gyr Disk age selected by the other binning regime (note also that 14 Gyr was the oldest curve available for fitting). Although it is difficult to resolve this matter satisfactorily with the current data set, there are two pertinent points to raise. The problem does not apply to the Wood models, the fits to which are extremely difficult to dislodge from the 9–11 Gyr region indicated by Figure 21 (a). Secondly, Wood and Oswalt (1998), as a result of their Monte Carlo analysis of the WDLF, recommend choosing a binning in which the crucial lowest luminosity bin contains ~ 5 objects; giving

a reasonable compromise between the requirements of good signal to noise in the final bin and having that bin as faint as possible to provide maximum information on the position of the cut off. This means a bin size of $1 M_{\text{bol}}$ for our data set, for which the fitted Disk age is well constrained for both models.

A brief investigation of the effect of altering the Disk scale height in Equation 13 revealed that for any scale height between 250 and 400 pc the alterations in space densities for a LF binned as in Table 5 are restricted to a few hundredths in $\log \phi$. Variations at this level have a negligible effect on the fits to model LFs. This behaviour is to be expected, since it is objects with large d_{max} which are most affected by changes in the scale height, and these make the smallest contributions to the space density when using the $1/V_{\text{max}}$ prescription.

An overview of all the various fittings to both sets of models points firmly to a Disk age between 9 and 11 Gyr using the Wood models, and an age of 12–14 Gyr using the GB models. This discrepancy is expected (LRB, García-Berro et al. 1997) and indicates the extent of errors introduced by uncertainties in the WD crystallisation process; the Wood model Disk age should be a reliable lower limit however, and Figure 21 demonstrates the difficulty in obtaining a Disk age of less than 9 Gyr from our data. We note that the Wood models seem to represent our data better, the GB models not following the peak in the observed LF. Wood (1992) reported that the uncertainties in the inputs to model WDLFs lead to a further ~ 1 Gyr contribution to the total error. Further insight into the error associated with the Disk age may be gained by considering the extremities of the distribution of atmosphere types within the sample. The 50% probability assigned to the H and He atmosphere is adopted in the absence of strong evidence for a dominant atmospheric type amongst the crucial coolest WDs (see eg. the coolest bin in Figure 1 of BRL), and has no physical basis. Adopting all H atmospheres leads to high space density estimates in the final LF bins and arbitrarily old Disk age estimates. More interestingly, a LF composed of all He atmosphere WDs is still incompatible with Disk ages below 8 Gyr, regardless of the model WDLF used. This reiterates the important point that the cosmologically interesting lower Disk age limit appears to be 8 Gyr, and that even a Disk as young as this must be considered unlikely (Figure 21). Our adopted Disk age estimation is therefore 10_{-1}^{+3} Gyr.

There are at least two possible effects arising from our present lack of extensive follow up observational data that could affect the derived Disk age. First, as may be seen in Figure 14 there is a small group of objects lying just beyond our RPMD cut-off that have not been included in our CWD sample. Although the distribution of known WDs on the RPMD (the BRL objects in Figure 18) indicates a population of CWDs is not expected in this region, the reason for this may be that many of the known CWDs have been themselves selected on the basis of RPM criteria (Luyten 1970). It may be that the region of the RPMD just beyond our cut-off has not been adequately investigated before, since in the presence of noisier data from blink comparators and eye-measure photometry it would be hopelessly confused. These considerations argue strongly for a wholesale spectroscopic survey using multi-fibre instruments of the entire population below $H_R = 19$ for complete confidence that our sample does

not exclude any CWDs. For the present, the possibility that a few more CWDs exist in our catalogue but do not satisfy our RPMD survey criteria cannot be ruled out. Such objects would certainly be very cool, resulting in a higher Disc age estimate. The second effect concerns the question of mass. The difficulty is amply demonstrated by the case of CWD ESO 439-26 (Ruiz et al. 1995), which was observed to have a luminosity fainter by 1 magnitude than the WDLF cut off. Analysis of the object’s optical energy distribution in conjunction with a measure of trigonometric parallax allowed the authors to conclude that its low luminosity was in fact due to its large mass, or small radius. Again, ideally it would be desirable to obtain parallaxes and CCD optical and IR photometry of our entire sample, obviating the need to assume a mass of $0.6M_{\odot}$ (and allowing the surface composition to be constrained).

In summary, our WD sample has passed every test for completeness applied to it. The calculated space density of WDs is slightly higher than that for the LDM sample, however we do not detect the much higher total space densities found by more recent authors (Ruiz 1995, Festin 1998). Our WDLF yields a Disc age estimate of 10_{+3}^{-1} Gyr, older but still consistent with previous estimates (Winget 1987, LRB, OSWH). In the context of current cosmochronometry, our Disc age estimate is consistent with current Globular cluster age estimates of 13-14Gyr (Vandenberg 1998). Finally, when combined only with a conservative 1 Gyr value for the halo-Disc formation interval (Burkert, Truran & Hensler 1992, Pitts & Tayler 1992) and a further 1 Gyr for the big bang-halo formation interval, a 10 Gyr Disc excludes $\Omega = 1$, $\Lambda = 0$ cosmologies based on current estimates for H_0 of 60-80 (Freedman 1998).

9 CONCLUSIONS

(i) Using a large collection of COSMOS/SuperCOSMOS digitised Schmidt plate data in ESO/SERC field 287 we have extracted a sample of proper motion objects. Number counts indicate this sample is complete down to the survey proper motion limit, which was chosen with care to exclude contaminant spurious proper motion measures.

(ii) A sample of cool white dwarfs have been culled from our proper motion objects using the reduced proper motion technique. By overplotting samples of known extreme subdwarfs we show our CWD sample is unlikely to be contaminated by other stellar population groups. We have confirmed the WD status of a number of our sample with AAT spectroscopy. The sample passes the (V/V_{max}) completeness test.

(iii) We calculate a total WD space density of 4.16×10^{-3} WDs per cubic parsec using Schmidt’s $(1/V_{max})$ method. Careful comparison of luminosity functions constructed from our sample and theoretical models indicate an age for the local Galactic Disc of 10_{+3}^{-1} Gyr, older than previous estimates using this technique.

ACKNOWLEDGMENTS

We would like to thank M. Wood and E. García-Berro for access to theoretical WDLFs, and P. Bergeron, P. Hauschildt

and B. Hansen for supplying model atmosphere predictions. Thanks also to S. Ryan for supplying lists of subdwarfs, and to Andy Taylor for useful discussions concerning statistics. This work would not have been possible without the time and expertise of the SuperCOSMOS and UK Schmidt Library staff. Particular thanks to Harvey MacGillivray, Mike Read and Sue Tritton. Richard Knox acknowledges a PPARC postgraduate studentship.

REFERENCES

- Beard S.M., MacGillivray H.T., Thanisch P.F., 1990, MNRAS, 247, 311
- Bergeron P., Wesemael F., Beauchamp A., 1995, PASP, 107, 1047
- Bergeron P., Ruiz M.T., Leggett S.K., 1997, ApJS, 108, 339
- Burkert A., Truran J.W., Hensler G., 1992, ApJ, 391, 651
- Evans D.W., 1989, A&AS, 78, 249
- Evans D.W., 1992, MNRAS, 255, 521
- Festin L., 1998, A&A, 336, 883
- Fleming T.A., Liebert J., Green R.F., 1986, ApJ, 308, 176
- Freedman W.L., 1998, in Turok N., ed., Proceedings for “Critical Dialogs in Cosmology”, in press (Princeton University Press) (preprint astro-ph 9612024)
- García-Berro E., Isern J., Hernanz M., 1997, MNRAS, 289, 973
- Giclas H.L., Burnham R., Thomas N.G., 1971, Lowell Proper Motion Survey, Northern Hemisphere Catalogue (Flagstaff: Lowell)
- Giclas H.L., Burnham R., Thomas N.G., 1978, Lowell Proper Motion Survey, Southern Hemisphere Catalogue Lowell Obs. Bull. 164, Vol VIII, p.89
- Greenstein J.L., Liebert J., 1990, ApJ, 360, 662
- Hambly N.C., Smartt S.J., Hodgkin S.T., 1997, ApJ, 489, L157
- Hambly N.C., Miller L., MacGillivray H.T., Herd J.T., Cormack, W.A., 1998, MNRAS, 298, 897
- Hansen B.M.S., 1998, Nature, 394, 860
- Hauschildt P.H., Allard F., Baron E., 1998, ApJ, in press
- Hawkins M.R.S., 1986, MNRAS, 223, 845
- Hawkins M.R.S., Bessell M.S., 1988, MNRAS, 234, 177
- Hawkins M.R.S., 1991, in IAU Commission 9: Working Group on Wide-Field Imaging, Newsletter No. 1, 23
- Hawkins M.R.S., Ducourant C., Jones H. R. A., Rapaport M., 1998, MNRAS, 294, 505
- Hernanz M., García-Berro E., Isern J., Mochkovitch R., Segretain L., Chabrier G., 1994, ApJ, 434, 652
- Isern J, Garcí-Berro E, Hernanz M., Mochkovitch R, Torres S, 1998, ApJ, 503, 239
- Jimenez R., Flynn C., Kotoneva E., 1998, MNRAS, 299, 515
- Kemp S.N., Meaburn J., 1993, A&A, 274, 19
- Knox R.A., Hambly N.C., Hawkins M.R.S., MacGillivray H.T., 1998, MNRAS, 297, 839
- Leggett S.K., Ruiz M.T., Bergeron P., 1998, ApJ, 497, 294
- Liebert J., Dahn C.C., and Monet D.G., 1988, ApJ, 332, 891
- Luyten W.J., 1969, Proper Motion Survey with the 48” Schmidt Telescope XXI (U. Minn)
- Luyten W.J., 1970, White Dwarfs, U. Minn
- Luyten W.J., 1974, Proper Motion Survey with the 48” Schmidt Telescope XXXVIII, U. Minn
- Luyten W.J., 1979, Proper Motion Survey with the 48” Schmidt Telescope LII, U. Minn
- Luyten W.J., 1979, LHS Catalogue, U. Minn
- MacGillivray H.T., Stobie R.S., 1984, Vistas in Astronomy, 27, 433
- Monet D.G., et al., 1992, AJ, 103, 638
- Oswalt T.D., Smith J.A., 1995, Koester D. & Werner K., eds., in White Dwarfs, Springer, Berlin, p.24

- Oswalt T.D., Smith J.A., Wood M.A., Hintzen P., 1996, *Nature*, 382, 692
 Pitts E., Tayler R.J., 1992, *MNRAS*, 255, 557
 Ruiz M.T., Takamiya M.Y., 1995, *AJ*, 109, 2817
 Ruiz M.T., Bergeron P., Leggett S.K., Anguita C., 1995, *ApJ*, 455, L159
 Ryan S.G., 1989, *AJ*, 98, 1693
 Schmidt M., 1959, *ApJ*, 129, 243
 Schmidt M., 1968, *ApJ*, 151, 393
 Schmidt M., 1975, *ApJ*, 202, 22
 Schwartzberg J.M., Phillipps S., Parker Q.A., 1996, *A&AS*, 117, 179
 Stobie R.S., Ishida K., Peacock J.A., 1989, *MNRAS*, 238, 709
 Tinney C.G., Reid I.N., Mould J.R., 1993, *ApJ*, 414, 254
 Vandenberg D.A., 1998, Bedding T. R., Booth A. J. & Davis J., eds., in *IAU Symp Fundamental Stellar Properties: The Interaction between Observation and Theory*, Kluwer, Dordrecht, p.439
 Véron P., Hawkins M.R.S., 1995, *A&A*, 296, 665
 Winget D.E., Hansen C.J., Liebert J., Van Horn H.M., Fontaine G., Nather R.E., Kepler S.O., Lamb D.Q., 1987, *ApJ*, 315, L77
 Wood M.A., 1992, *ApJ*, 386, 539
 Wood M.A., 1995, Koester D. & Werner K., eds., in *White Dwarfs*, Springer, Berlin, p.41
 Wood M.A., Oswalt, T.D., 1998, *ApJ*, 497, 870

This paper has been produced using the Royal Astronomical Society/Blackwell Science L^AT_EX style file.

APPENDIX A: REDUCED PROPER MOTION DIAGRAMS

The reduced proper motion (RPM) is defined by

$$H = m + 5 \log_{10} \mu + 5 \quad (\text{A1})$$

where m is apparent magnitude and μ proper motion. A reduced proper motion diagram (RPMD) is a plot of colour against RPM. It is a powerful way of combining proper motions and photometry to distinguish stellar population groups. Equation A1 can be re-written using the relationships $m = M - 5 + 5 \log d$ and $\mu = V_T/4.74d$ to give

$$H = M + 5 \log_{10} V_T - 3.379 \quad (\text{A2})$$

where M is the absolute magnitude, V_T the transverse velocity (in kms^{-1}) and d the distance. Since M and V_T are both intrinsic properties of the star, so too is H .

To see the significance of H , suppose that every star had an identical V_T ; H would then clearly be simply M plus a constant and the distribution of a particular population group in H at a particular colour would depend solely on the spread of the populations' colour-magnitude relation at that colour. Of course there is a distribution in $5 \log_{10} V_T$ for each population, but since the tangential velocities are distributed around a most probable value the RPM serves as an estimate of M , ie. $M = a + bH$ (a and b constants). The resulting locus for each population in the RPMD is then the convolution of its colour magnitude distribution with its $5 \log_{10} V_T$ distribution over the diagrams colour range. To allow population discrimination in some colour region we therefore only require that the various population loci do not overlap significantly in that region of the RPMD. In effect the RPMD is analogous to the Hertsprung-Russell diagram, and in both plots the white dwarf population is quite distinct in most colours.